

# On-Chip Multidimensional Manipulation of Far-Field Radiation with Guided Wave-Driven Metasurfaces

Yuebian Zhang, Zhancheng Li, Wenwei Liu, Hua Cheng,\* Duk-Yong Choi,\* Jianguo Tian, and Shuqi Chen\*

Miniaturization and integration of multiple optical components in one chip are important trends in the future development of optical chips. Despite various on-chip multifunctional metasurfaces having been proposed, simultaneously manipulating the polarization and wavefront of far-field radiation still remains a challenge. Here, a novel approach to simultaneously realize on-chip polarization and wavefront manipulation of far-field radiation with guided wave-driven geometric metasurfaces is theoretically proposed and experimentally demonstrated. Various polarized beams with controllable radiation angles can be generated by maneuvering phase gradients and far-field interferences of meta-atoms. The phase and amplitude of off-chip radiation can be tailored all at once by altering the rotation angles and positions of each meta-atom. As a proof of concept, a guided wave-driven metalens and four different on-chip polarization generators are fabricated and characterized. These on-chip devices work at broadband and can realize mode-dependent beam deflection. This study provides a practical route toward on-chip multidimensional control of far-field radiation, which could support a further step in the development of photonic integrated circuits, wearable near-eye displays, and optical information processing devices, just to name a few.

on-chip optical applications such as integrated quantum optics,<sup>[1]</sup> photon switching,<sup>[2]</sup> and optical communications.<sup>[3]</sup> For many applications, it is desirable to connect the free-space light and on-chip wave fields in waveguides, such as in photodetectors,<sup>[4]</sup> advanced lasers,<sup>[5]</sup> and augmented reality devices.<sup>[6]</sup> Although conventional grating couplers can be used to couple light into or out of waveguides,<sup>[7,8]</sup> this method has limited ability to manipulate the off-chip light field. In particular, it is challenging for grating couplers to control the polarization states or arbitrarily shape the complex amplitude of the off-chip light field. Another way to realize coupling between free-space light and guided waves is to integrate subwavelength artificial microstructures (also called “meta-atoms”) with waveguides.<sup>[9]</sup> Due to the unique resonance and scattering properties of meta-atoms, directional out-coupling of guided waves,<sup>[10]</sup> on-chip polarization (de)multiplexing,<sup>[11]</sup> and many novel on-chip applications have been proposed in recent years.<sup>[12,13]</sup>

## 1. Introduction


Nanophotonic waveguides play a vital role in photonic integrated circuits, and they represent an attractive platform for novel

Metasurfaces are two-dimensional meta-atom arrays that can realize more complex wave field manipulations.<sup>[14–18]</sup> By changing the geometrical parameters and arrangements of the meta-atoms in metasurfaces, polarization converters,<sup>[19]</sup> beam deflectors,<sup>[20]</sup> metalenses,<sup>[21]</sup> holograms,<sup>[22,23]</sup> coding metasurfaces,<sup>[24]</sup> and other novel applications have been demonstrated to control free-space light.<sup>[25–29]</sup> In the past few years, by combining metasurfaces on waveguides or microcavities, on-chip metalenses,<sup>[30,31]</sup> mode converters,<sup>[32,33]</sup> waveguide metacouplers,<sup>[34–38]</sup> and some off-chip wavefront shaping metasurfaces<sup>[39–45]</sup> have been proposed. Fang et al. demonstrated that slab waveguide-integrated metasurfaces are capable of beam focusing, multichannel vortex beam generation and holography based on the geometric phase design.<sup>[46]</sup> Recently, several on-chip multifunctional metasurfaces have been presented based on the detour phase.<sup>[47–49]</sup> However, it is difficult to simultaneously manipulate the phase and polarization of the radiation in these designs. Meanwhile, only the fundamental transverse-electric (TE) mode is used as incident light, which limits the possibility of achieving polarization- or mode-dependent multifunctional devices.

Y. Zhang, Z. Li, W. Liu, H. Cheng, J. Tian, S. Chen  
The Key Laboratory of Weak Light Nonlinear Photonics, Ministry of Education, Smart Sensing Interdisciplinary Science Center, Renewable Energy Conversion and Storage Center, School of Physics and TEDA Institute of Applied Physics  
Nankai University  
Tianjin 300071, China  
E-mail: hcheng@nankai.edu.cn; schen@nankai.edu.cn

D.-Y. Choi  
Laser Physics Centre, Research School of Physics  
Australian National University  
Canberra, ACT 2601, Australia  
E-mail: duk.choi@anu.edu.au

S. Chen  
The Collaborative Innovation Center of Extreme Optics  
Shanxi University  
Taiyuan, Shanxi 030006, China

 The ORCID identification number(s) for the author(s) of this article can be found under <https://doi.org/10.1002/lpor.202300109>

DOI: 10.1002/lpor.202300109

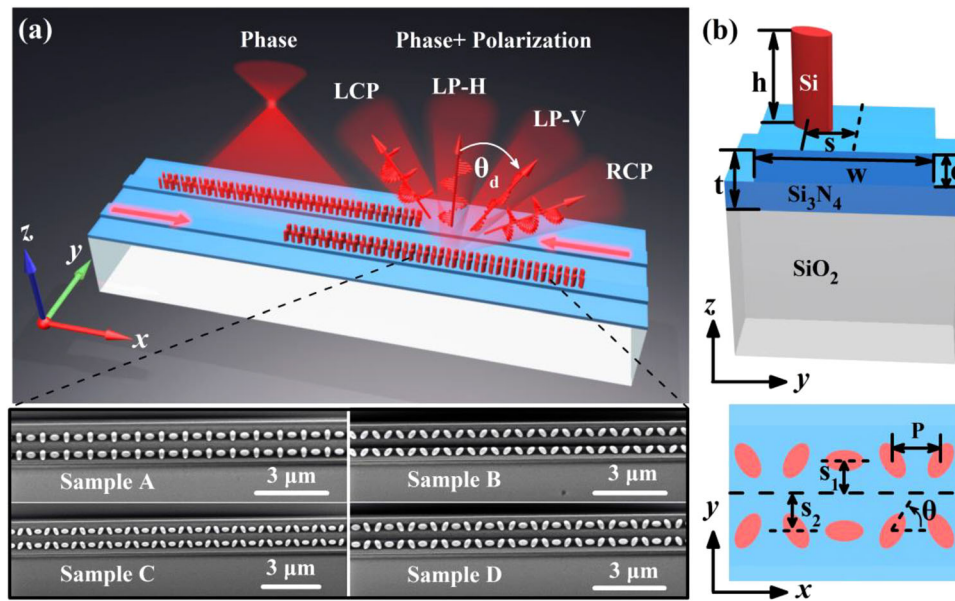


**Figure 1.** a) Schematic of the guided wave-driven geometric metasurfaces. The metasurfaces are excited by guided waves and radiate different polarized light with controllable radiation angles. The inset shows SEM images of the fabricated samples that can produce off-chip LP along vertical (LP-V) (sample A), horizontal (LP-H) (sample B), circularly polarized (sample C), and non-uniformly polarized (sample D) light. The nanopillar spacing of samples A and B is  $P = 480$  nm, while that of samples C and D is  $P = 450$  nm. b) Three-dimensional (3D) view of a unit cell (upper) and plan view of the silicon nanostructures (lower). The black dashed lines bisecting the waveguide mark the position  $y = 0$ .  $s$  is the lateral offset of the nanopillar relative to the center of the waveguide.  $s_1$  and  $s_2$  are the  $y$ -coordinates of the nanopillar arrays.

In this paper, we can convert waveguide modes into free space light fields and simultaneously manipulate their polarization and wavefront. Different polarized beams with controllable radiation angles can be generated by tailoring the phase gradients and far-field interferences of the meta-atoms. A guided wave-driven metasurfaces and four different on-chip polarization generators are fabricated and characterized to validate the phase and polarization manipulation abilities of the guided wave-driven geometric metasurfaces. They can work at broadband and enable both large and small angle deflections. Compared with previous guided wave-driven metasurfaces (GWDMs) based on slab waveguides,<sup>[45–49]</sup> our approach explored the lateral offset of the meta-atoms, which provides a new degree of freedom to easily control the amplitude of radiated light. Moreover, it supports several types of incident modes, which can be explored for mode-dependent beam deflection and other functions. This work finds a feasible route toward on-chip multidimensional manipulation of far-field radiation.

## 2. Results and Discussion

The designed GWDMs and scanning electron microscope (SEM) images of the fabricated samples are shown in **Figure 1**. The metasurfaces can be excited by guided waves and radiate distinct polarized light with controllable radiation angles. It consists of a  $\text{SiO}_2$  substrate, a  $\text{Si}_3\text{N}_4$  ridge waveguide and two rows of hydrogenated amorphous silicon ( $\alpha$ -Si:H) elliptical nanopillar arrays. The waveguide has width  $w = 1500$  nm and thickness  $t = 570$  nm. The etching depth of the waveguide is  $d = 300$  nm. The major and minor axis and height of each elliptical silicon nanopillar are  $a = 390$  nm,  $b = 210$  nm, and  $h = 850$  nm, respectively. The dis-

tance between two adjacent nanopillars along the  $x$ -axis is  $P$ . The  $y$ -coordinates of the nanopillar arrays are  $s_1$  and  $s_2$ .

Since TE guided waves can be decomposed into in-plane left-handed circularly polarized (LCP) and right-handed circularly polarized (RCP) components, Pancharatnam–Berry (PB) phase of the GWDMs can be realized with the incident TE modes of the ridge waveguide. We simulated the phase and the electric field intensity  $|E|^2$  of the scattered wave from a single silicon nanopillar on a  $\text{Si}_3\text{N}_4$  waveguide. **Figure 2a,b** represents the outcome as a function of orientation angle  $\theta$  for fundamental TE mode incidence. The phase of the scattered RCP light can be altered from  $-\pi$  to  $\pi$  by spatially rotating the elliptical nanopillar. As the incident mode is not circularly polarized, which is nearly linearly polarized light at the center of the waveguide and right-handed or left-handed elliptically polarized light at positions where  $y \neq 0$ , the scattered RCP light contains both the unconverted RCP component and the polarization converted from the LCP. As a result, the phase change is affected by the unconverted RCP component and deviates from  $\varphi = 2\theta$ . When the nanopillar is closer to the center of the waveguide, the effect of the unconverted light on the phase is greater (more details can be found in Figure S1, Supporting Information). We therefore used a silicon nanopillar with a lateral offset  $s = 500$  nm to study the PB phase of the scattered RCP light in Figure 2a. The scattered electric field intensity from the nanopillar also varies with its orientation, nearly proportional to  $\sin^2\theta$  (Figure 2b). This is comprehensible since the resonance within the nanostructure is mainly excited by the electric field component along the major axis of the elliptical nanopillar. When the orientation angle of the nanopillar changes, the intersection angle between the input electric field and the major axis of structure changes accordingly. Furthermore, the scattered field

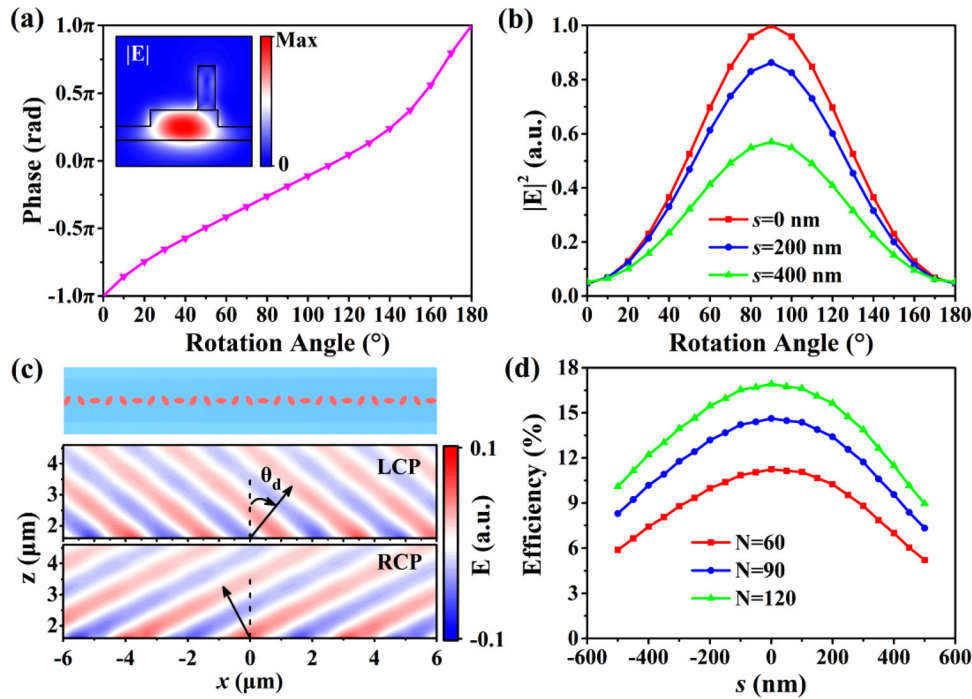


**Figure 2.** Simulated a) phase of the RCP component and b) electric field intensity  $|E|^2$  of the scattered wave from a single silicon nanopillar patterned on a  $\text{Si}_3\text{N}_4$  waveguide as a function of orientation angle  $\theta$ . The input light is fundamental TE mode with a wavelength of 1550 nm. The inset in (a) shows the electric field amplitude in the waveguide and silicon nanopillar, which has a lateral offset  $s = 500$  nm relative to the center of the waveguide. c) Simulated electric field distributions of the LCP component,  $E_{\text{LCP}}$ , and RCP component,  $E_{\text{RCP}}$ , in the  $x$ - $z$  plane bisecting the waveguide for a one-row array comprising 120 nanopillars. The incident light is the fundamental TE mode at 1550 nm. Top is the nanopillar array used in the simulation, which is patterned on the midline of the waveguide and has a distance  $P = 480$  nm between adjacent nanopillars. d) Up-extraction efficiency as a function of array position  $s$  for the on-chip beam deflector comprising different numbers of nanopillars  $N$ .

intensity from the nanopillar can be manipulated by varying the lateral offset of the nanostructure. As shown in Figure 2b, the scattered field will decrease with the increase of the lateral offset  $s$ , coinciding with the electric field distribution of the  $\text{TE}_{00}$  waveguide mode (see the inset in Figure 2a). Because the electric field intensity of the  $\text{TE}_{00}$  mode has a maximum at the center of the waveguide and decreases along the lateral direction, the scattered field intensity from the nanopillar also decreases when the nanopillar moves toward the waveguide edge. This provides a simple way to manipulate the amplitude of the scattered light. To evaluate the amplitude modulation capability of a single nanopillar, we defined the modulation depth of the nanopillar structure as  $1 - (|E|_{\text{min}}^2 / |E|_{\text{max}}^2)$ , with  $|E|_{\text{min}}^2$  and  $|E|_{\text{max}}^2$  being the minimum and maximum electric field intensities of the scattered wave from a single nanopillar patterned on waveguide. If we keep the orientation angles  $\theta = 90^\circ$  and change the lateral offsets of the nanopillars, the modulation depth is about 65%, which is limited by the sizes of the waveguide and the nanopillars. However, it can reach 95.3% by altering the orientation angles of the nanopillars.

To validate the PB phases of the waveguide-integrated nanostructures, we designed a guided wave-driven beam deflector that deflects RCP and LCP beams to different off-chip directions. Figure 2c illustrates the deflector containing one row of 120 nanopillars patterned on the midline of the waveguide. The orientation angles of the nanopillars are varied along the  $x$ -direction with a step of  $\pi/3$  to generate a constant phase gradient. According to

the generalized Snell's laws,<sup>[15]</sup> the anomalous diffraction of the GWDM obeys the following equation :

$$k_0 \sin \theta_d = n_{\text{eff}} k_0 - m \frac{2\pi}{P} + \frac{d\Phi}{dx} \quad (1)$$

where  $k_0 = 2\pi/\lambda_0$  is the vacuum wavevector,  $\theta_d$  is the diffraction angle in free space,  $n_{\text{eff}}$  is the effective refractive index of the waveguide mode and can be obtained from simulation,  $m$  is the diffraction order due to the spacing of the meta-atoms, and  $d\Phi/dx$  is the phase gradient provided by the geometric metasurface.  $\Phi = 2\sigma\theta$  is the phase change of the scattered circularly polarized light due to the PB phase. When the GWDM shown in Figure 2c is excited by the  $\text{TE}_{00}$  mode at 1550 nm, the nanopillar array provides a phase gradient  $d\Phi/dx = \pm 2\pi/3P$  for the RCP and LCP scattered lights. As a consequence, their diffraction angles for the  $m = 1$  order RCP and  $m = 0$  order LCP light are  $-27.3^\circ$  and  $38.1^\circ$ , respectively. Figure 2c represents the simulated electric field distributions of the LCP and RCP components in the  $x$ - $z$  plane bisecting the  $\text{Si}_3\text{N}_4$  waveguide. It is obvious that the LCP and RCP beams are extracted from the waveguide and deflected to different directions with distinct angles, which agrees well with the theoretical prediction. We also simulated the up-extraction efficiencies of the on-chip beam deflectors as a function of array position  $s$  and nanopillar numbers  $N$ . Here, the efficiency is defined as the ratio of the power recorded by a power monitor at 3.5  $\mu\text{m}$

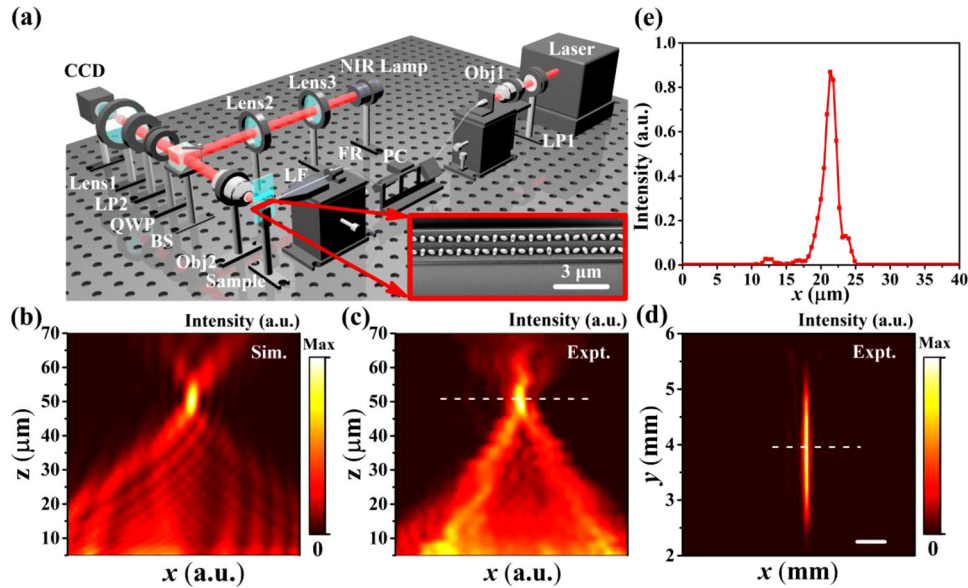


**Figure 3.** a) Illustration of the measurement setup for characterizing the off-chip light deflection in Fourier space and focusing in real space. Lens 1 is not used in the off-chip light focusing measurement. LP, linear polarizer; QWP, quarter-wave plate; Obj, objective; PC, polarization controller; FR, fiber rotator; LF, lensed fiber; BS, beam splitter. The auxiliary optical path with an NIR lamp is used to obtain the image of the sample and assist in aligning the sample with the lensed fiber. The inset shows the SEM image of the fabricated guided wave-driven metalens. The b) simulated and c) measured LCP intensity distributions along the propagation direction of the off-chip light. The white dashed line in (c) shows the position of the focal plane. The incident light is the  $TE_{00}$  mode with a wavelength of 1550 nm. d) Measured LCP intensity distributions at the focal plane. Scale bar: 1 mm. e) Measured LCP intensity distributions along the white dashed line in (d). The abscissa was calibrated by dividing it by the magnification of the imaging system.

above the metasurface to the incident power  $\eta = P_{\text{monitor}}/P_{\text{in}}$ . Figure 2d clearly shows that the up-extraction can increase with the increase of the nanopillar numbers and be managed by changing the positions of the nanopillar arrays. Owing to the electric field distribution of the fundamental TE mode in the ridge waveguide, the extraction efficiency of the beam deflector reaches a maximum when the nanopillar array is on the centerline of the waveguide. The maximum number of the nanopillars is related to the scattering efficiency of a single nanopillar. A higher scattering efficiency can reduce the footprint (total number of the nanopillars) of the metasurface. If the scattering efficiency of a single nanopillar is too high, the light field in waveguide will decay fast. As a result, the up-extraction amplitude will dramatically decrease along the propagation direction of the waveguide mode, which will degrade the performance of the device. In addition, mode conversion may occur if the scattering efficiencies of the meta-atoms are too high. In our design, we chose a moderate scattering efficiency to balance the device performance and footprint. All these results clearly show that the phase and amplitude of the off-chip radiation can be simultaneously manipulated by changing the rotation angles and positions of each meta-atom.

To experimentally validate the PB phases of the waveguide-integrated nanostructures, we designed and fabricated a guided wave-driven metalens that functions as off-chip light focusing. The metalens contains two rows of a-Si:H elliptical nanopillar arrays to improve the up-extraction efficiencies, which are located at positions  $s = \pm 350$  nm with the same orientation angle arrangement, as depicted in the inset in Figure 3a. Each row has  $N = 161$  nanopillars, and the distance between two adjacent silicon nanopillars is  $P = 480$  nm. The rotation angles of

the nanopillars are  $\theta(x) = [k_0(\sqrt{x^2 + f^2} - f) + n_{\text{eff}}k_0x]/2$ , where  $f = 50$   $\mu\text{m}$  is the focal length of the metalens at the design wavelength 1550 nm,  $x$  is the  $x$ -coordinate of the nanopillar, and  $x = 0$  is taken at the midpoint of the nanopillar arrays. The PB phase of the LCP scattered light provided by the nanopillar arrays can be expressed as

$$\Phi(x) = -k_0(\sqrt{x^2 + f^2} - f) - n_{\text{eff}}k_0x \quad (2)$$

Combined with the propagation phase of the guided wave, the total phase of the LCP scattered light along the  $x$ -direction is  $\Phi(x) + n_{\text{eff}}k_0x = -k_0(\sqrt{x^2 + f^2} - f)$ , which can focus the up-extracted LCP light in free space with a focal length  $f$ . An optical setup was built to measure the focusing of the guided wave-driven metalens, as shown in Figure 3a. An infrared laser beam was generated from a supercontinuum laser source (NKT Photonics) and then converted to  $y$ -polarized light. Then, the light was coupled into the on-chip ridge waveguide in an end-fire manner by using a lensed fiber. The off-chip light was collected by an objective and finally recorded by an infrared camera. The simulated and measured LCP intensity distributions along the propagation direction of the off-chip light are illustrated in Figure 3b,c, respectively. It can be clearly seen that the off-chip scattered light is focused at about 50  $\mu\text{m}$  from the guided wave-driven metalens, which agrees well with the simulation. It is noteworthy that the guided wave-driven metalens operates at a wideband as the PB phases of the nanopillars are broadband (more details can be found in Figure S2, Supporting Information). Figure 3d,e shows the LCP intensity distributions at the focal plane. The scattered light is well focused in the  $x$  direction but spreads out in the  $y$



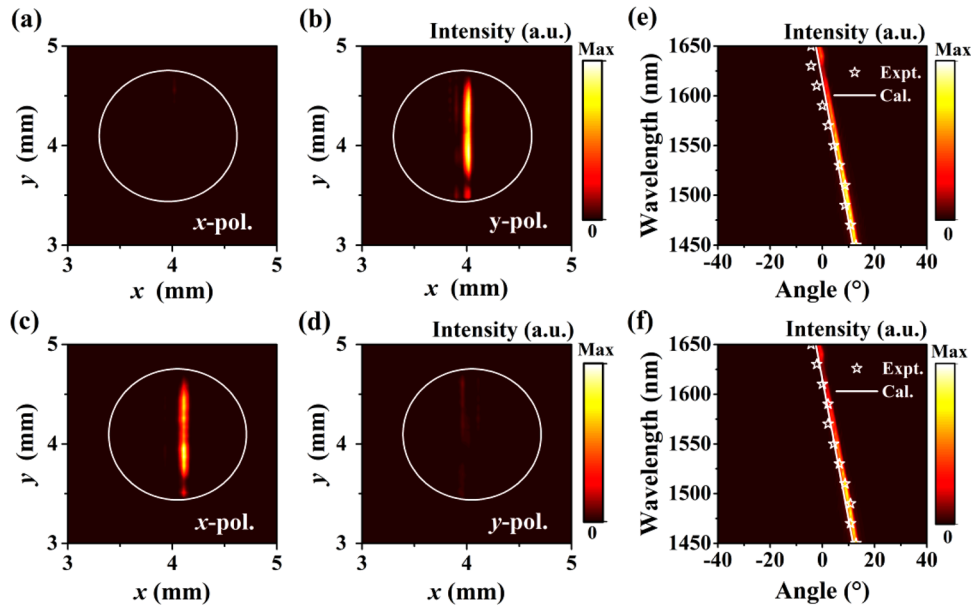


**Figure 4.** Measured Fourier plane images of the a) *x*-polarized and b) *y*-polarized light radiated from sample A. The white circles correspond to the maximum angular field of view. Measured Fourier plane images of the c) *x*-polarized light and d) *y*-polarized light radiated by sample B. e) Measured (white star), calculated (white line), and simulated (color map) radiation angles of sample A at different wavelengths. The color bar represents the simulated far-field radiation intensities of the outgoing beams that have  $k_y = 0$ . f) Measured, calculated, and simulated radiation angles of sample B at different wavelengths.

direction because no phase modulation is applied in this direction. The measured full-width at half-maximum in the *x* direction is  $\approx 1.93 \mu\text{m}$ , which is slightly larger than the simulated result ( $1.4 \mu\text{m}$ ) due to the fabrication and measurement imperfections.

As the phase and amplitude of the off-chip radiation can be simultaneously manipulated, the proposed GWDMs are highly suitable for achieving on-chip polarization generators. An arbitrary state of polarization (SoP)  $|n\rangle$  can be synthesized by two orthogonal circularly polarized components:

$$|n\rangle = A_R |R\rangle + A_L e^{i2\delta} |L\rangle \quad (3)$$

where  $|R\rangle$  and  $|L\rangle$  represent the RCP and LCP lights.  $A_R$  and  $A_L$  are the amplitude coefficients of the RCP and LCP components;  $2\delta = \varphi_L - \varphi_R$  is the phase difference between them. The main axis angle  $\psi$  and ellipticity angle  $\chi$  can be derived as  $\psi = \delta$  and  $\chi = \sin^{-1}[(A_R^2 - A_L^2)/(A_R^2 + A_L^2)]/2$ . The phase and amplitude of the off-chip scattered circularly polarized light could be controlled at will by the rotation angles and positions of each meta-atoms, respectively; therefore, we can engineer the SoP of the off-chip light from the GWDMs. One way for combining the RCP and LCP scattered lights is to set  $d\Phi/dx = \pm\pi/P$ , which can deflect them in the same direction from only one row of the nanopillar array. Equation (1) can be written as  $\sin\theta_d = n_{\text{eff}} - \lambda_0/2P$  (when “+” is taken,  $m = 1$ , and when “-” is taken,  $m = 0$ ). The calculated diffraction angles are about  $4.6^\circ$  for both RCP and LCP beams at  $1550 \text{ nm}$ . Each elliptical nanopillar can be viewed as a dipole antenna that radiates light polarized along the major axis of the nanopillar. By varying the orientation angles of two elliptical nanopillars in each period and maintaining their relative angles to  $90^\circ$ , various polarized light can be generated and diffracted at the same angles (more details can be found in Figure S3, Support-

ing Information). We fabricated two samples that enable off-chip light deflection and polarization manipulation simultaneously (see samples A and B in Figure 1a), each of which consists of two rows of Si nanopillar arrays. The nanopillar spacing of each sample is  $P = 480 \text{ nm}$ . The nanopillars of sample A are alternately arranged with orientation angles  $\theta = 0^\circ/90^\circ$ . Sample B is similar to sample A, but the orientation angles are  $\theta = 45^\circ/135^\circ$ . Two samples can couple the guided waves into the air at the same deflection angle but with orthogonal polarizations. To measure the SoP and the deflection angles, we used the homebuilt optical setup shown in Figure 3a to characterize the far-field intensity distributions in Fourier space. The GWDMs were positioned on the focal plane of a  $50\times$  objective lens, and the far-field intensity distributions in Fourier space were captured by an infrared camera. The off-chip diffraction angles of the samples were obtained by measuring the lateral coordinates of the diffracted beams in the sensor plane  $x_{\text{sensor}}$ , which is proportional to  $\tan\theta_d$ .<sup>[50]</sup> Figure 4a,b shows the measured Fourier space images of the *x*- and *y*-polarized lights radiated from sample A. The off-chip diffraction beam from sample A is mainly *y*-polarized (LP-V) light, whilst that from sample B is mainly *x*-polarized (LP-H) light, as evident in Figure 4c,d. These results can be understood by analyzing the far-field interferences of the scattered light between two adjacent meta-atoms are  $\Delta\varphi_{\text{prop}} = k_0(n_{\text{eff}}P - P\sin\theta_d) = \pi$ . For sample A, the scattered electric field intensity is predominantly from the nanopillars with orientation angle  $\theta = 90^\circ$ , as demonstrated in Figure 2b. Therefore, the far-field of sample A is mainly *y*-polarized light. At the same token, there is a  $\pi$  propagation phase difference for each two adjacent meta-atoms under the  $\text{TE}_{00}$  mode excitation in sample B. As a consequence, the *y*- and *x*-polarization components interfere destructively and

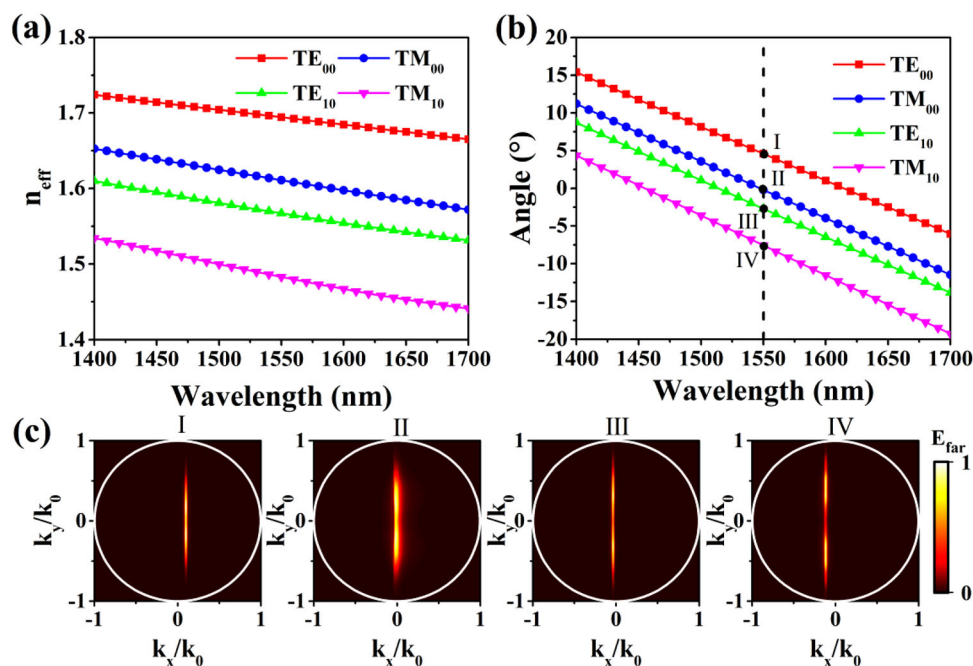


**Figure 5.** The dependence of radiation properties on the incident modes. a) Simulated effective refractive indices of different waveguide modes. b) Calculated radiation angles of sample A excited by different incident modes. c) Simulated electric field distributions in  $k$ -space of sample A excited by different incident modes at 1550 nm. I–IV correspond to the points shown in (b).

constructively in the far-field, respectively; therefore, the far-field of sample B is mainly  $x$ -polarized light. Figure 4e,f shows the measured radiation angles from samples A and B at different wavelengths, which fits well with the calculated and simulated results even though the slight mismatch is likely to be incurred from the fabrication and measurement imperfections. The radiation angles decrease with increase of the wavelength and gradually change from positive to negative angles when the incident wavelengths are varied from 1450 to 1650 nm. This is because the effective refractive index  $n_{\text{eff}}$  of the waveguide mode decreases with increase of the wavelength. Figure 4e,f also clearly demonstrates that the on-chip deflectors are operational at broad bandwidths, which is the attribute of the PB phase employed in the current design.

According to Equation (1), the deflection angles of the radiated light can be changed by tailoring the effective refractive index  $n_{\text{eff}}$  of the waveguide mode. If we use different waveguide modes to excite the ridge waveguide-integrated metasurfaces, we can easily manipulate the deflection angles of the radiated light. **Figure 5a** shows the simulated effective refractive indices of four different waveguide modes in a bare ridge waveguide. Obviously, the effective refractive indices decrease with wavelength, and those of the TM modes are smaller than those of the TE modes at 1550 nm. Consequently, the deflection angles decrease with wavelength and can be gradually changed from positive to negative angles when the wavelengths vary from 1400 to 1700 nm, which is verified by **Figure 5b** and the experimental results (see **Figure 4e**). From **Figure 5b**, it is also possible to modify the radiation angles from positive to negative with incident waveguide modes. **Figure 5c** shows the simulated electric field distributions in  $k$ -space of sample A under different incident modes at 1550 nm, which

fits well with the calculated results in **Figure 5b**. It can be clearly seen that the off-chip light is deflected to the right and left sides of the normal for  $\text{TE}_{00}$  and  $\text{TE}_{10}$  modes, respectively. This property gives us a convenient way to dynamically control the radiation angles. In the experiment, the incident waveguide mode can be easily changed from  $\text{TE}_{00}$  mode to  $\text{TM}_{00}$  mode by changing the polarization state of the incident light.

Another way to combine RCP and LCP scattered lights is to use the photonic spin Hall effect (PSHE) to separate the RCP and LCP components, and then use two rows of nanopillar arrays to deflect them to the same angle so that they can superpose in the far-field. As a proof of concept, a GWDM carrying out off-chip PSHE under waveguide mode excitation was designed and fabricated (sample C in **Figure 1a**). It contains two rows of nanopillar arrays, each of which comprises 161 nanopillars patterned at the positions  $s_1 = 350$  nm and  $s_2 = -350$  nm. The orientation angles of the nanopillars are linearly varied along the  $x$ -direction with a step size of  $\pi/3$  to generate a constant phase gradient. **Figure 6a,b** shows the measured Fourier space images of the RCP and LCP lights radiated by sample C. The RCP and LCP beams are deflected in the  $k-(k_x < 0)$  and  $k+(k_x > 0)$  directions respectively, which clearly demonstrates the realization of the PSHE. **Figure 5c** depicts the measured radiation angles of sample C at different wavelengths, which fit well with the calculated and simulated results. The radiation angle of the RCP light increases with increase of the wavelength, while the LCP light has an opposite trend, which can be derived from Equation (1). To further prove the validity of our approach, i.e., the manipulation of the SoP of the off-chip light with the GWDMs, we fabricated sample D, which can generate a non-uniform polarization distribution through the combination of RCP and LCP

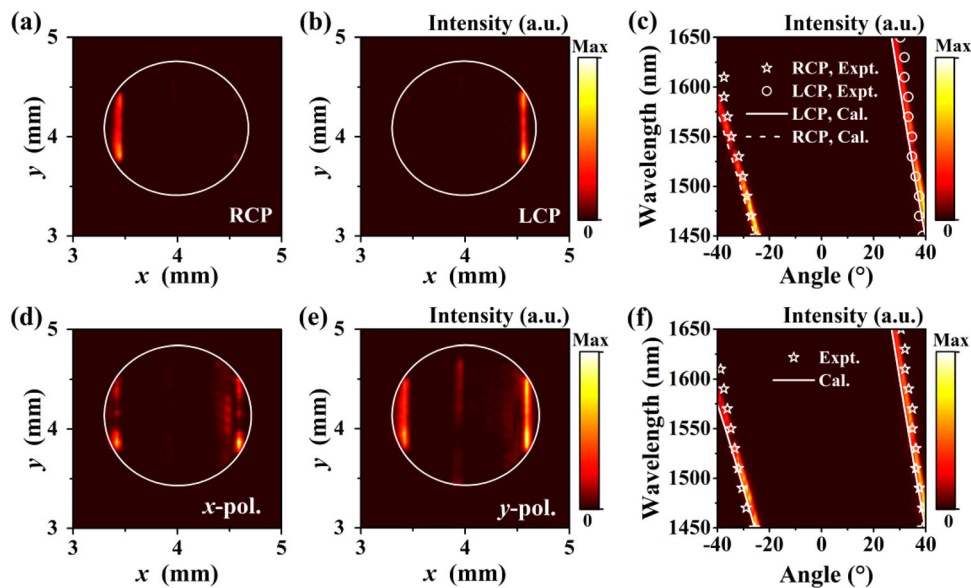


**Figure 6.** Measured Fourier plane images of the a) RCP and b) LCP light radiated by sample C. c) Measured, calculated, and simulated (color map) radiation angles of sample C at different wavelengths. Measured Fourier plane images of the d) x-polarized and e) y-polarized light radiated from sample D. f) Measured, calculated, and simulated radiation angles of sample D at different wavelengths.

scattered lights. As represented in Figure 1a, it has the same second row nanopillar arrangement as sample C, but the orientation angles of the nanopillars at  $s_1 = 350$  nm are linearly varied with a step size of  $-\pi/3$  so that opposite circularly polarized light can be deflected to the same angle. Because the incident light of the GWDM sample is the  $TE_{00}$  waveguide mode, the phase difference between the RCP and LCP beams deflected to the same angle is  $\pi$ . According to Equation (3), it is obvious that the SoP of the generated far-field directly above the waveguide is  $\gamma$ -polarization. When the scattered light gradually deviates from the  $x$ - $z$  plane bisecting the ridge waveguide, the phase difference gradually deviates from  $\pi$ , so the SoP will gradually deviate from  $\gamma$ -polarization along the  $y$  direction and the  $x$ -polarized component will appear. Figure 6d,e shows the measured Fourier space images of the  $x$ - and  $y$ -polarized lights radiated from sample D. The off-chip radiated light from sample D is mainly  $\gamma$ -polarized when  $k_y = 0$ , but the SoP deviates from  $\gamma$ -polarization when  $k_y$  increases, which is consistent with the theoretical analysis and the simulation results. Figure 6f shows the measured deflection angles of the  $\gamma$ -polarized light radiated from sample D at different wavelengths, which fit well with the calculated and simulated results. Compared with Figure 6c, we can find that the deflection angles of the light radiated from samples C and D are the same, but the SoPs are different. According to Equation (1), the deflection angles can be easily manipulated by tailoring the effective refractive index  $n_{\text{eff}}$  of the waveguide mode and the nanopillar spacing  $P$ , which is also validated by the simulation (more details can be found in Figure S4, Supporting Information). Compared with previous slab waveguide-based metasurfaces (see Table S1, Supporting Information for more details about the comparison between our work and other literatures), our approach provides more degrees of freedom to control the radiated light and supports more types of incident modes, which can be explored for mode-dependent beam deflection and other functions. These results prove that the

proposed GWDMs can function as on-chip wideband polarization generators with controllable deflection angles.

### 3. Conclusions and Outlook

In conclusion, we theoretically propose and experimentally demonstrate a novel approach to convert waveguide modes into free space light with controllable polarization states and phase gradients based on GWDMs. By integrating subwavelength nanostructures with on-chip ridge waveguides, more design freedoms are introduced and on-chip multidimensional manipulation of far-field radiation can be realized. For example, the amplitude of the off-chip scattered light can be manipulated by tailoring the lateral offset of the nanopillars and the nanopillar numbers; the phase gradients of the nanopillar arrays can be controlled by spatially rotating the nanopillars and changing the nanopillar spacing. In principle, the amplitude, phase and polarization of the off-chip scattered light can be controlled simultaneously based on our method. Both large- and small-angle deflection (vertical radiation) have been achieved by choosing different design strategies. Furthermore, the proposed GWDMs can work at broadband and be dynamically tuned by changing the incident polarization and waveguide modes. In view that the proposed GWDMs are based on ridge or rectangular waveguides, they can be expanded easily into GWDM arrays with different functions to realize polarization multiplexing or some more complex applications. The proposed GWDMs could also be integrated with microfluidic channels<sup>[51]</sup> and used in refractive index sensing or on-chip dynamic light field control.<sup>[52]</sup> This study finds a feasible route toward on-chip multidimensional manipulation of far-field radiation, which may provide a further step in the development of photonic integrated circuits, wearable near-eye displays, optical encryption and optical information processing devices.

## 4. Experimental Section

**Sample Fabrication:** A 570 nm  $\text{Si}_3\text{N}_4$  film was deposited on the  $\text{SiO}_2$  substrate via plasma-enhanced chemical vapor deposition (PECVD) and was partially etched to pattern the ridge waveguides. Then, a 20 nm  $\text{Al}_2\text{O}_3$  protective layer was deposited on the  $\text{Si}_3\text{N}_4$  waveguide to protect the waveguides during the silicon nanopillar etching step. Subsequently, an 850 nm-thick hydrogenated amorphous silicon (a-Si:H) layer was deposited from the Oxford PECVD system. The elliptical holes of resist patterns were then produced by electron beam lithography, and 70 nm thick Al was deposited by e-beam evaporation (Temescal BJD-2000), accompanied by a lift-off process in which the sample was soaked in a resist remover (ZDMAC from ZEON Co.). The nanopillars were formed by reactive ion plasma etching using  $\text{CHF}_3$  and  $\text{SF}_6$  gas mix, followed by the residual Al removal by an Al wet etchant (a mixture of  $\text{H}_3\text{PO}_4$ ,  $\text{HNO}_3$ , acetic acid, and water).

**Optical Measurement:** The collimated near-infrared (NIR) laser beam generated from a supercontinuous laser source (NKT SuperK EXR-20) passed through an infrared polarizer and then was coupled into a fiber with an objective (Sigma NIR plan apo 10 $\times$ , NA = 0.3). A polarization controller and a fiber rotator were used to control the polarization of the input light. The light was coupled into the on-chip ridge waveguide in an end-fire manner by using a polarization-maintaining lensed fiber mounted on a 3D translational stage. For the measurement of the focusing in real space, the off-chip light was collected by an objective (50 $\times$ /0.67) and then transmitted through a quarter-wave plate and a linear polarizer and recorded by an infrared camera. The objective, quarter-wave plate, linear polarizer, and infrared camera were all integrated on an XYZ translation stage with a high-resolution piezo-controlled actuator in the z-direction. By moving the z stage, the real-space images ( $x$ - $y$  plane) were taken at different distances from the waveguide plane. The auxiliary optical path with an NIR lamp was used to obtain the image of the sample and assist in aligning the sample with the lensed fiber. When the Fourier plane images were measured, the GWDMS were placed on the focal plane of a 50 $\times$  objective lens, and the far-field intensity distributions in Fourier space were imaged by a lens and captured by an infrared camera (photographs of the measurement setup can be found in Figure S5, Supporting Information).

**Numerical Simulation:** The numerical simulations were conducted by using a finite difference time-domain (FDTD) approach based on the Lumerical Solutions commercial software package. In this software, the phase of an electromagnetic wave increases with propagation length and decreases with time. The phase and electric field intensity  $|E|^2$  of the scattered wave shown in Figure 2a,b are recorded by a point monitor at  $z = 3000$  nm directly above the nanopillar. The optical constants of amorphous silicon were taken from ref. [53]. The refractive indices of the  $\text{SiO}_2$  substrate and  $\text{Si}_3\text{N}_4$  were 1.44 and 1.927, respectively. To reduce the memory required for the simulation,  $N = 121$  nanopillars were used in the simulation of the metalens and polarization generators. The scattered light fields of the GWDMS were recorded by a planar monitor at  $z = 5$   $\mu\text{m}$  directly above the waveguide to calculate the far-field radiation angles shown in Figures 3 and 4.

## Supporting Information

Supporting Information is available from the Wiley Online Library or from the author.

## Acknowledgements

This work was supported by the National Key Research and Development Program of China (2021YFA1400601 and 2022YFA1404501), the National Natural Science Fund for Distinguished Young Scholars (11925403), the National Natural Science Foundation of China (12122406, 12192253, 11974193, 12274237, 12274239, 12104243, and U22A20258), and the China Postdoctoral Science Foundation (2020M680851). The metasurface nanofabrication was performed at the ACT node of the Australian National Fabrication Facility.

## Conflict of Interest

The authors declare no conflict of interest.

## Data Availability Statement

The data that support the findings of this study are available from the corresponding author upon reasonable request.

## Keywords

metasurfaces, on-chip polarization generators, wave field multidimensional manipulation, waveguides

Received: February 5, 2023

Revised: April 5, 2023

Published online:

- [1] L.-T. Feng, M. Zhang, Z.-Y. Zhou, M. Li, X. Xiong, L. Yu, B.-S. Shi, G.-P. Guo, D.-X. Dai, X.-F. Ren, G.-C. Guo, *Nat. Commun.* **2016**, *7*, 11985.
- [2] A. Javadi, D. Ding, M. H. Appel, S. Mahmoodian, M. C. Löbl, I. Söllner, R. Schott, C. Papon, T. Pregolato, S. Stobbe, L. Midolo, T. Schröder, A. D. Wieck, A. Ludwig, R. J. Warburton, P. Lodahl, *Nat. Nanotechnol.* **2018**, *13*, 398.
- [3] L.-W. Luo, N. Ophir, C. P. Chen, L. H. Gabrielli, C. B. Poitras, K. Bergmen, M. Lipson, *Nat. Commun.* **2014**, *5*, 3069.
- [4] S. J. Kim, J.-H. Kang, M. Mutlu, J. Park, W. Park, K. E. Goodson, R. Sinclair, S. Fan, P. G. Kik, M. L. Brongersma, *Nat. Commun.* **2018**, *9*, 316.
- [5] Y. Li, J. Zhang, D. Huang, H. Sun, F. Fan, J. Feng, Z. Wang, C. Z. Ning, *Nat. Nanotechnol.* **2017**, *12*, 987.
- [6] G. A. Koulueris, K. Akşit, M. Stengel, R. K. Mantiuk, K. Mania, C. Richardt, *Comput. Graph. Forum* **2019**, *38*, 493.
- [7] C.-S. Im, B. Bhandari, K.-P. Lee, S.-M. Kim, M.-C. Oh, S.-S. Lee, *Opt. Express* **2020**, *28*, 3270.
- [8] S. Kim, D. A. Westly, B. J. Roxworthy, Q. Li, A. Yulaev, K. Srinivasan, V. A. Aksyuk, *Light: Sci. Appl.* **2018**, *7*, 72.
- [9] D. Vercrucy, P. Neutens, L. Lagae, N. Verellen, P. Van Dorpe, *ACS Photonics* **2017**, *4*, 1398.
- [10] F. B. Arango, A. Kwadrin, A. F. Koenderink, *ACS Nano* **2012**, *6*, 10156.
- [11] R. Guo, M. Decker, F. Setzpfandt, X. Gai, D. Y. Choi, R. Kiselev, A. Chipouline, I. Staude, T. Pertsch, D. N. Neshev, Y. S. Kivshar, *Sci. Adv.* **2017**, *3*, e1700007.
- [12] K. G. Cognée, H. M. Doeleman, P. Lalanne, A. F. Koenderink, *ACS Photonics* **2020**, *7*, 3049.
- [13] F. J. Rodríguez-Fortuño, A. Espinosa-Soria, A. Martínez, *J. Opt.* **2016**, *18*, 123001.
- [14] P. C. Wu, W.-Y. Tsai, W. T. Chen, Y.-W. Huang, T.-Y. Chen, J.-W. Chen, C. Y. Liao, C. H. Chu, G. Sun, D. P. Tsai, *Nano Lett.* **2017**, *17*, 445.
- [15] N. Yu, P. Genevet, M. A. Kats, F. Aieta, J.-P. Tetienne, F. Capasso, Z. Gaburro, *Science* **2011**, *334*, 333.
- [16] S. Chen, W. Liu, Z. Li, H. Cheng, J. Tian, *Adv. Mater.* **2020**, *32*, 1805912.
- [17] S. Chen, Z. Li, Y. Zhang, H. Cheng, J. Tian, *Adv. Opt. Mater.* **2018**, *6*, 1800104.
- [18] Y. Zhang, H. Liu, H. Cheng, J. Tian, S. Chen, *Opto-Electron. Adv.* **2020**, *3*, 200002.
- [19] N. Yu, F. Aieta, P. Genevet, M. A. Kats, Z. Gaburro, F. Capasso, *Nano Lett.* **2012**, *12*, 6328.
- [20] L. Huang, X. Chen, H. Muhlenbernd, G. Li, B. Bai, Q. Tan, G. Jin, T. Zentgraf, S. Zhang, *Nano Lett.* **2012**, *12*, 5750.
- [21] M. Khorasaninejad, F. Capasso, *Science* **2017**, *358*, 8100.



- [22] X. Chen, L. Huang, H. Muhlenbernd, G. Li, B. Bai, Q. Tan, G. Jin, C.-W. Qiu, S. Zhang, T. Zentgraf, *Nat. Commun.* **2012**, *3*, 1198.
- [23] W. Wan, J. Gao, X. Yang, *Adv. Opt. Mater.* **2017**, *5*, 1700541.
- [24] J. Y. Dai, L. X. Yang, J. C. Ke, M. Z. Chen, W. Tang, X. Li, M. Chen, Z. H. Wu, Q. Cheng, S. Jin, T. J. Cui, *Laser Photonics Rev.* **2020**, *14*, 1900133.
- [25] S. Chen, Z. Li, W. Liu, H. Cheng, J. Tian, *Adv. Mater.* **2019**, *31*, 1802458.
- [26] Z. Wang, C. Qian, Z. Fan, H. Chen, *Adv. Sci.* **2023**, *10*, 2204699.
- [27] C. Qian, X. Lin, X. Lin, J. Xu, Y. Sun, E. Li, B. Zhang, H. Chen, *Light: Sci. Appl.* **2020**, *9*, 59.
- [28] C. Qian, Z. Wang, H. Qian, T. Cai, B. Zheng, X. Lin, Y. Shen, I. Kaminer, E. Li, H. Chen, *Nat. Commun.* **2022**, *13*, 2694.
- [29] L. Li, K. Yao, Z. Wang, Y. Liu, *Laser Photonics Rev.* **2020**, *14*, 1900244.
- [30] Z. Wang, T. Li, A. Soman, D. Mao, T. Kananen, T. Gu, *Nat. Commun.* **2019**, *10*, 3547.
- [31] Y. Fan, X. L. Roux, A. Korovin, A. Lupu, A. de Lustrac, *ACS Nano* **2017**, *11*, 4599.
- [32] Z. Li, M.-H. Kim, C. Wang, Z. Han, S. Shrestha, A. C. Overvig, M. Lu, A. Stein, A. M. Agarwal, M. Lončar, N. Yu, *Nat. Nanotechnol.* **2017**, *12*, 675.
- [33] L. Deng, Y. Xu, R. Jin, Z. Cai, Y. Liu, *Adv. Opt. Mater.* **2022**, *10*, 2200910.
- [34] A. Pors, S. I. Bozhevolnyi, *Phys. Rev. Appl.* **2016**, *5*, 064015.
- [35] Y. Meng, F. Hu, Z. Liu, P. Xie, Y. Shen, Q. Xiao, X. Fu, S. H. Bae, M. Gong, *Opt. Express* **2019**, *27*, 16425.
- [36] Y. Zhang, Z. Li, W. Liu, Z. Li, H. Cheng, S. Chen, J. Tian, *Adv. Opt. Mater.* **2019**, *7*, 1801273.
- [37] Y. Zhang, Z. Li, W. Liu, Z. Li, H. Cheng, J. Tian, S. Chen, *Opt. Lett.* **2021**, *46*, 3528.
- [38] Y. Meng, Z. Liu, Z. Xie, R. Wang, T. Qi, F. Hu, H. Kim, Q. Xiao, X. Fu, Q. Wu, S.-H. Bae, M. Gong, X. Yuan, *Photonics Res.* **2020**, *8*, 564.
- [39] P.-N. Ni, P. Fu, P.-P. Chen, C. Xu, Y.-Y. Xie, P. Genevet, *Nat. Commun.* **2022**, *13*, 7795.
- [40] Y. Meng, Y. Chen, L. Lu, Y. Ding, A. Cusano, J. A. Fan, Q. Hu, K. Wang, Z. Xie, Z. Liu, Y. Yang, Q. Liu, M. Gong, Q. Xiao, S. Sun, M. Zhang, X. Yuan, X. Ni, *Light: Sci. Appl.* **2021**, *10*, 235.
- [41] X. Guo, Y. Ding, X. Chen, Y. Duan, X. Ni, *Sci. Adv.* **2020**, *6*, 4142.
- [42] P.-Y. Hsieh, S.-L. Fang, Y.-S. Lin, W.-H. Huang, J.-M. Shieh, P. Yu, Y.-C. Chang, *Nanophotonics* **2022**, *11*, 4687.
- [43] Y. Ha, Y. Guo, M. Pu, X. Li, X. Ma, Z. Zhang, X. Luo, *Adv. Theory Simul.* **2021**, *4*, 2000239.
- [44] Y. Ding, X. Chen, Y. Duan, H. Huang, L. Zhang, S. Chang, X. Guo, X. Ni, *ACS Photonics* **2022**, *9*, 398.
- [45] Z. Huang, D. L. Marks, D. R. Smith, *Optica* **2019**, *6*, 119.
- [46] B. Fang, Z. Wang, S. Gao, S. Zhu, T. Li, *Nanophotonics* **2021**, *11*, 1923.
- [47] R. Yang, S. Wan, Y. Shi, Z. Wang, J. Tang, Z. Li, *Laser Photonics Rev.* **2022**, *16*, 2200127.
- [48] Y. Shi, C. Wan, C. Dai, S. Wan, Y. Liu, C. Zhang, Z. Li, *Optica* **2022**, *9*, 670.
- [49] Y. Shi, C. Wan, C. Dai, Z. Wang, S. Wan, G. Zheng, S. Zhang, Z. Li, *Laser Photonics Rev.* **2022**, *16*, 2100638.
- [50] J. Bar-David, U. Levy, *Nano Lett.* **2019**, *19*, 1044.
- [51] Q. Li, J. van de Groep, A. K. White, J.-H. Song, S. A. Longwell, P. M. Fordyce, S. R. Quake, P. G. Kik, M. L. Brongersma, *Nat. Nanotechnol.* **2022**, *17*, 1097.
- [52] G.-B. Wu, J. Y. Dai, Q. Cheng, T. J. Cui, C. H. Chan, *Nat. Electron.* **2022**, *5*, 808.
- [53] E. D. Palik, Ed, *Handbook of Optical Constants of Solids*, Academic Press, San Diego, CA, USA **1998**.